Giant Magnetic Anisotropy in the Atomically Thin van der Waals Antiferromagnet FePS₃

Youjin Lee, Suhan Son, Chaebin Kim, Soonmin Kang, Junying Shen, Michel Kenzelmann, Bernard Delley, Tatiana Savchenko, Sergii Parchenko, Woongki Na, Ki-Young Choi, Wondong Kim, Hyeonsik Cheong, Peter M. Derlet, Armin Kleibert,* and Je-Geun Park*

Van der Waals (vdW) magnets are an ideal platform for tailoring 2D magnetism with immense potential for spintronics applications and are intensively investigated. However, little is known about the microscopic origin of magnetic order in these antiferromagnetic systems. X-ray photoemission electron microscopy is used to address the electronic and magnetic properties of the vdW antiferromagnet FePS₃ down to the monolayer. The experiments reveal a giant out-of-plane magnetic anisotropy of 22 meV per Fe ion, accompanied by unquenched magnetic orbital moments. Moreover, the calculations suggest that the Ising magnetism in FePS₃ is a visible manifestation of spin–orbit entanglement of the Fe 3d electron system.

1. Introduction

The history of 2D magnetism is rich with exciting theoretical and experimental breakthroughs, starting from the Onsager solution of the 2D Ising Hamiltonian,[1] which has given a strong theoretical basis and motivation to realise 2D magnetic systems. The discovery of magnetic van der Waals (vdW) materials is thus an important new development,[2,3] which is also expected to play an essential role in much wider research fields such as nanotechnology and spintronics.[4,5] For instance, vdW magnetic materials offer a natural platform to investigate the fundamentals of 2D magnetism and their possible applications, including spintronics, by providing natural magnetic materials with atomic thickness. Specifically, the

new class of vdW magnets provides the long-sought-after experimental testbeds of the fundamental Hamiltonians of 2D magnetism: Ising, XY, and Heisenberg models.[6] The first experimental test of the Onsager solution of the Ising model was performed on antiferromagnetic FePS₃,[7] followed by the discovery of 2D ferromagnetic van der Waals materials such as CrGeTe₃[8] and CrI₃.[9] Eventually, the XY and Heisenberg models were subsequently realized using NiPS₃,[10,11] CrCl₃,[12] and MnPS₃,[13–15] respectively.

The investigation of vdW materials has so far focused on 2D magnetic order phenomena, and much less attention has been paid to their microscopic origin. Typically, the role of orbital magnetism is often neglected since the magnetic orbital moment is supposedly quenched in most 3d transition metal based magnetic materials via so-called crystal field splittings due to the interaction with the surrounding atoms. However, systems with reduced symmetry can, in principle, host sizeable magnetic orbital moments approaching those of the respective free atoms.[16,17] In such a case, the spin–orbit interaction can give rise to new phenomena such as spin–orbit entanglement, a manifestation of direct quantum effects in the condensed matter state.[18] Moreover, FePS₃ is—as we will show—a material whose properties are dominated by strong electron correlations. In spin–orbit entangled systems, electron spins and orbital motions

Y. Lee, S. Son, C. Kim, J.-G. Park
Center for Quantum Materials
Seoul National University
Seoul 08826, Republic of Korea
E-mail: jgpark10@snu.ac.kr
Y. Lee, S. Son, C. Kim, S. Kang, K.-Y. Choi, J.-G. Park
Department of Physics and Astronomy, Institute of Applied Physics
Seoul National University
Seoul 08826, Republic of Korea

The ORCID identification number(s) for the author(s) of this article can be found under https://doi.org/10.1002/aelm.202200650.

J. Shen, M. Kenzelmann
Laboratory for Neutron Scattering and Imaging
Paul Scherrer Institut
Villigen PSI CH-5232, Switzerland
B. Delley, P. M. Derlet
Condensed Matter Theory Group
Paul Scherrer Institut
Villigen PSI CH-5232, Switzerland
T. Savchenko, S. Parchenko, A. Kleibert
Swiss Light Source
Paul Scherrer Institut
Villigen PSI CH-5232, Switzerland
E-mail: armin.kleibert@psi.ch
W. Na, H. Cheong
Department of Physics
Sogang University
Seoul 04107, Republic of Korea
W. Kim
Korea Research Institute of Standards and Science (KRISS)
Daejeon 34113, Republic of Korea

are locked in an entangled Hilbert space, leading to novel magnetic phenomena such as Kitaev physics.[19] Realizing and tuning such an entangled state would provide fundamentally new functionality to magnetic materials. Thus far, spin–orbit entanglement has been primarily considered in compounds containing heavy elements such as Ru, Ir, and 4f lanthanides.[20] However, such efforts have been relatively less vigorously made for 3d transition metals, let alone the important class of 2D vdW magnets. At this point, one may be better reminded that a standard model of magnetism would predict an almost negligible effect of the spin–orbit coupling on the magnetism of the 3d transition metal element simply because it is too small: it is on the order of 15–20 meV for Fe metal.

In this work, we shed important light on the role of orbital magnetism and, in particular, spin–orbit entanglement in the prototypical 2D Ising-type antiferromagnet $FePS_3$, which persists down to the monolayer limit. In addition to the fundamental interest, understanding antiferromagnetic 2D vdW materials such as $FePS_3$ is important for developing bourgeoning antiferromagnetic spintronics.[21,22] Thus far, the investigation of antiferromagnetic 2D vdW materials has been plagued by the lack of adequate experimental tools, which can directly probe the magnetic moments of few-layer thin antiferromagnetic samples at the nanometer scale.[23] This unfortunate situation about antiferromagnetic vdW materials is in stark contrast with atomically thin ferromagnetic materials, directly measured via the magneto-optical Kerr effect (MOKE)[8,9] and, more recently, diamond nitrogen-vacancy (NV) magnetometry.[24] To date, Raman[11,14] and second harmonic generation (SHG)[25] techniques have been used to study the 2D magnetism of atomically thin antiferromagnetic vdW materials. A recent transport measurement using the spin Hall magnetoresistance (SMR) succeeded in measuring the sublattice magnetization of exfoliated $FePS_3$,[26] which is another direction for the studies of vdW antiferromagnets. Although they prove practical, there are also limitations, as they cannot provide direct information about the microscopic origin of the antiferromagnetic properties.

Here, we use X-ray photoemission electron microscopy (XPEEM) in combination with X-ray absorption (XA) spectroscopy and the X-ray magnetic linear dichroism (XMLD) effect at the Fe L_3 edge to investigate the electronic and magnetic state of $FePS_3$ with atomic monolayer sensitivity and nanometer spatial resolution.[27–29] $FePS_3$ exhibits antiferromagnetic Ising-type order down to the monolayer regime, as demonstrated using Raman spectroscopy.[7] Here, we show that the Ising-type behavior is due to a giant magnetic single-ion anisotropy, which stabilizes the out-of-plane orientation of the magnetic moments even far above the Néel temperature. As the origin of this extraordinarily high anisotropy, we identify large unquenched orbital moments of ≈1 μ_B per Fe ion. Atomistic multiplet calculations reveal the exotic nature of the ground state of Fe^{2+} ions in $FePS_3$. Despite the smallness of the spin–orbit coupling strength, we find that the ground state of the six 3d electrons in $FePS_3$ is characterized by completely mixed spin and orbital wave functions. Such an unfactorizable mixture of spin and orbital states is a manifestation of multi-electron spin–orbit entanglement. Our results demonstrate that quantum spin–orbit entanglement should be considered an essential part of 2D vdW magnets to explore their full potential for fundamental research and applications.

$FePS_3$ is an Ising-type antiferromagnet with spin moments parallel to the $c*$-axis[30] in a honeycomb lattice with a zig-zag configuration (**Figure 1**a). Magnetic susceptibility
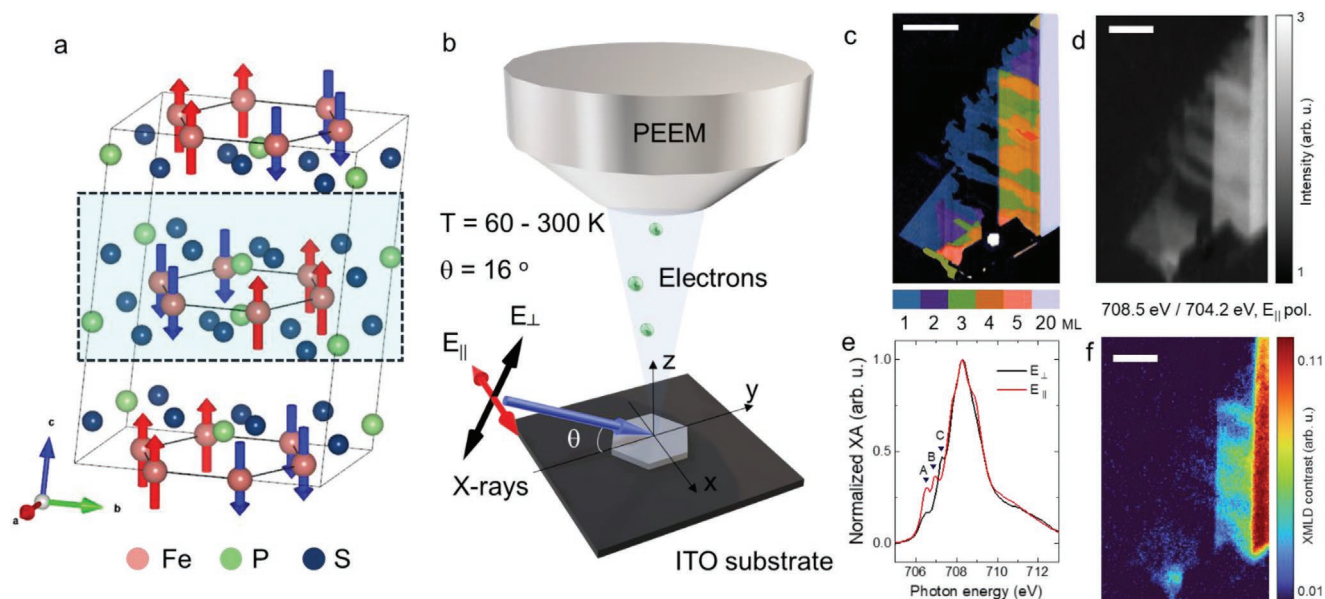

Figure 1. Schematic of the atomic structure of $FePS_3$ and the experimental setup. a) The magnetic moments are ordered in a zig-zag chain direction parallel to the $c*$-axis (red and blue arrows). The sky-blue shadow highlights the monolayer structure of $FePS_3$. b) Schematic of the XPEEM measurements with linearly polarized X-rays ($E_\parallel$ and $E_\perp$) exciting the sample at a grazing angle (16°). c) False-color AFM image of the exfoliated $FePS_3$ flake on an ITO support. Each color corresponds to a given number of $FePS_3$ monolayers, as shown in the color bar. d) XPEEM elemental contrast map of the same $FePS_3$ flake. e) Normalized XA spectra at the Fe L_3 edge were extracted from a 20 ML thick region of the $FePS_3$ sample for both polarizations. Three prepeaks are denoted as A, B, and C. f) Corresponding XMLD asymmetry map. The data in (d)–(f) are obtained at 65 K, below T_N. The scale bars are 5 μm.
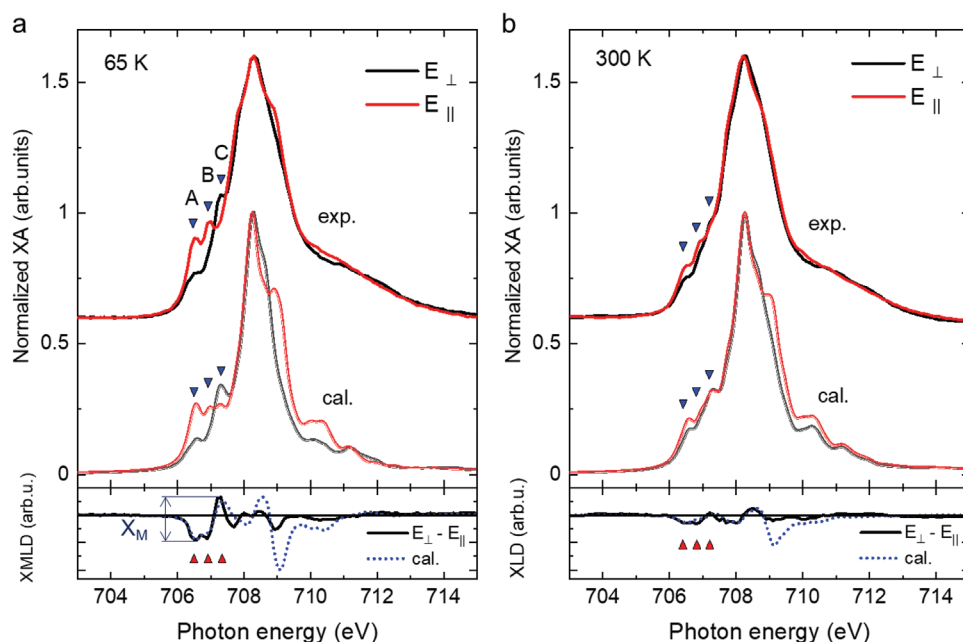
Figure 2. a,b) XA spectra of 20 ML-thick FePS$_3$. Data are taken at 65 K (a) and 300 K (b). The experimental (upper) and theoretical (lower) XA spectra for E$_\parallel$ (red) and E$_\perp$ (black). The experimental XA spectra are shifted by 0.6 upward for a better comparison. The corresponding experimental (black) and calculated (blue dotted) XMLD spectra are shown at the bottom.

measurements and neutron scattering data revealed a large magnetic out-of-plane anisotropy in bulk FePS$_3$.[30,31] The Ising-type behavior and the magnetic easy axis were confirmed using a torque magnetometer for bulk FePS$_3$.[32] The strong out-of-plane anisotropy, in principle, should be sufficient to enable Ising-type magnetic order in the individual 2D FePS$_3$ layers.[1] Indeed, stable antiferromagnetic order was observed in a single monolayer of FePS$_3$ using Raman spectroscopy.[7] However, the degree of magnetic order and the role of the interface with the substrate remain unclear because of the rather indirect spectroscopic Raman detection of antiferromagnetic order via magnon excitation and the related complex interplay between photons, phonons, and magnons.[33] Moreover, the microscopic origin of the out-of-plane anisotropy remains unclear despite its fundamental importance. Interestingly, recent theoretical work suggested that the out-of-plane anisotropy might be associated with significant magnetic orbital moments in FePS$_3$.[34] Although the density functional (DFT) calculation found a sizeable magnetic anisotropy by including spin–orbit coupling, experimental verification remained elusive. More importantly, the possibly entangled nature of the electronic ground state is completely unexamined.

2. XPEEM Investigations of the Ising Magnet FePS$_3$

To investigate the magnetic and electronic properties of FePS$_3$ with monolayer sensitivity we perform polarization-dependent XA spectroscopy and microscopy at the Fe $L_{2,3}$ edge employing XPEEM in the experimental geometry shown in Figure 1b. In this geometry the difference in the XA spectra recorded with the two orthogonal polarizations ($\mathbf{E}_\parallel$ and $\mathbf{E}_\perp$, respectively), i.e.,

the XMLD effect, is a measure of the local antiferromagnetic order. The normalized XMLD asymmetry X_M (see **Figure 2**a) is proportional to $\langle M_z^2 \rangle - \langle M_x^2 \rangle$, with $\langle M_{z,x}^2 \rangle$ being the expectation values of the squared order parameter perpendicular or parallel to the sample plane (see the Experimental Section). Before the experiment, FePS$_3$ flakes are exfoliated onto an indium tin oxide (ITO) substrate, which serves as electrically conductive support for the XPEEM investigations. Figure 1c shows an atomic force microscopy (AFM) image of a typical FePS$_3$ flake with micrometer-sized flat regions ranging from 1 to 20 monolayers (ML). The corresponding XPEEM elemental contrast map is displayed in Figure 1d. The XA spectra in Figure 1e were extracted from a 20 ML region of the FePS$_3$ sample for the two orthogonal polarizations recorded at 65 K, well below the Néel temperature $T_N = 118$ K of bulk FePS$_3$. The polarization-dependent XA spectra exhibit three distinct features, denoted as A, B, and C, associated with the XMLD effect due to the magnetically ordered state below T_N. Finally, the local magnetic order of the FePS$_3$ flake is visualized using XMLD contrast maps (Figure 1f). The figure shows the magnetic order to persist down to the monolayer (see also Figure S5, Supporting Information).

3. Comparison with Multiplet Calculations and Monte Carlo Simulations

We start our analysis by comparing the temperature-dependent XPEEM data of 20 ML FePS$_3$ with multiplet calculations and Monte Carlo (MC) simulations. Figure 2a,b shows the experimental XA spectra of 20 ML FePS$_3$ recorded at 65 and 300 K below and above T_N, respectively (see the Experimental Section for details). The linear dichroism in the spectra is significantly

larger below T_N than in the paramagnetic phase. The small remaining dichroic signal in the paramagnetic state reflects a nonmagnetic contribution due to the low symmetry of the trigonally distorted FeS_6 octahedra in $FePS_3$, present in all temperature regions.

To obtain further insight into the origin of the magnetism and magnetic order of $FePS_3$, we simulated the XA spectra using ligand field multiplet theory (see the Experimental Section). As shown in Figure 2a,b, our multiplet calculations performed for 65 and 300 K successfully reproduce the key features of the experimental XA and XMLD spectra. The multiplet calculations yield a spin moment $\langle S_z \rangle = 1.75 \pm 0.04$ and a large orbital moment $\langle L_z \rangle = 1.02 \pm 0.04$ per Fe ion, consistent with earlier DFT results.[34] Notably, these numbers compare well to those of Fe^{2+} ions in a d^6 high spin state with unquenched $S = 2$ and $\tilde{L} = 1$. For such a case, significant magnetic orbital moments are expected to give rise to a high magnetic anisotropy.[35]

To assess the magnetic anisotropy in $FePS_3$, we evaluate X_M as a function of temperature and compare these experimental data to the $\langle M_z^2 \rangle - \langle M_x^2 \rangle$ obtained from ensemble-averaged Monte Carlo (MC) simulations, as shown in **Figure 3**a, for 20 ML. The MC simulations are based on a classical 2D honeycomb lattice of the Heisenberg exchange model with strong local out-of-plane anisotropy (see the Experimental Section). Using an intra-ML exchange coupling corresponding to a ground state out-of-plane exchange field of $J = 15$ meV and an out-of-plane single-ion anisotropy of $K = 22$ meV, we successfully reproduce the known Néel temperature of 115 K and the experimental XMLD amplitude data, X_M (see Figure 3a). The exchange and anisotropy values compare well to those deduced from earlier theoretical predictions.[34,36] The high magnetic anisotropy is further consistent with the anisotropic magnetic susceptibility seen in bulk $FePS_3$ above T_N (Figure S1, Supporting Information). The positive sign of K further confirms the out-of-plane orientation of the magnetic moments, suggesting that the Ising-type magnetic order is an intrinsic property of the 2D layers of bulk $FePS_3$. It should be noted that the magnitude of the magnetic anisotropy estimated above is much larger, if not one of the largest, than in most other magnetic materials.[16]

4. Thickness Dependence of Magnetic Anisotropy

By taking advantage of the spatial resolution and sensitivity of XPEEM, we apply the same magnetic anisotropy analysis to sample regions with different thicknesses to reveal the role of interlayer and interface interactions. Fitting the temperature-dependent experimental data X_M with calculated $\langle M_z^2 \rangle - \langle M_x^2 \rangle$ with varying K at fixed J (Figures S3 and S4, Supporting Information), we find practically the same bulk-like behavior and properties persisting down to 4 ML. Below 4 ML, we observe a significant drop in the normalized asymmetry X_M at low temperature indicating some kind of change in the magnetic properties. The change in the magnetic properties is accompanied with changes in the XA spectra, which are most apparent in the monolayer (Figure 3c), which we can assign to an electron transfer from the ITO substrate to the first $FePS_3$ layers as discussed further below (see also the Supporting Information).
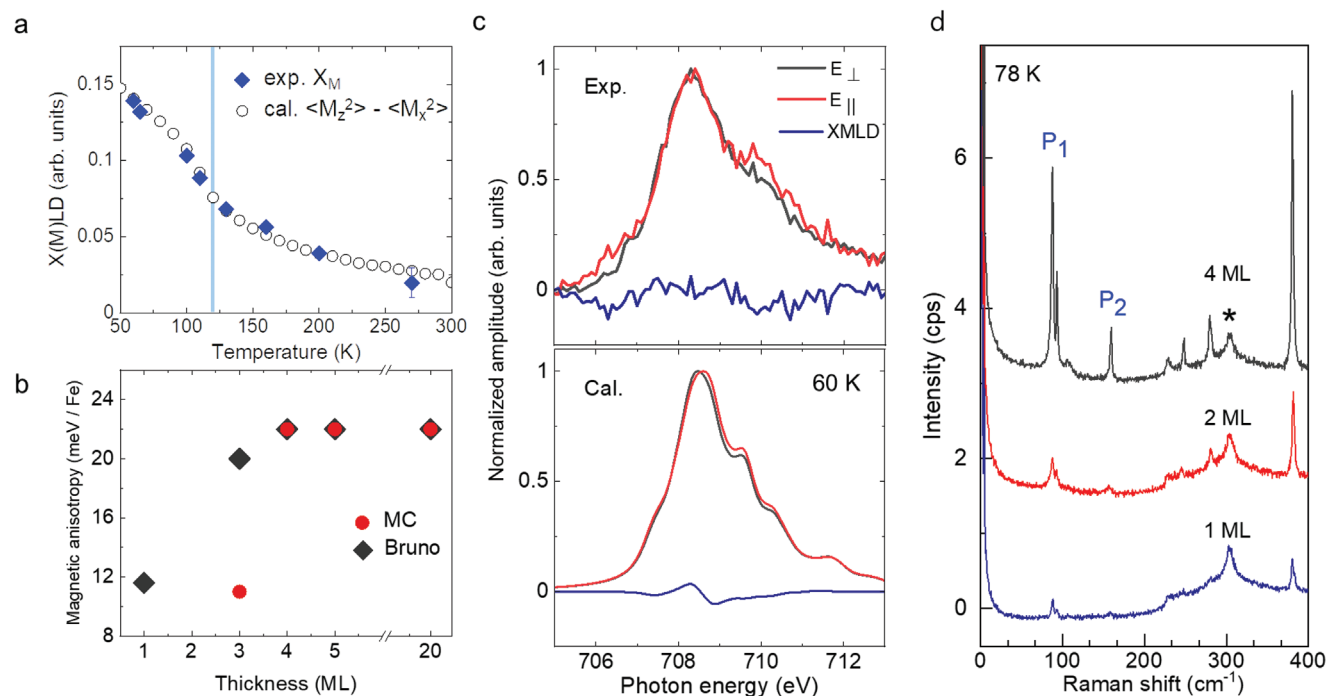

Figure 3. Thickness dependency of the magnetic anisotropy. a) Experimental XMLD amplitude X_M (blue diamonds) together with $\langle M_z^2 \rangle - \langle M_x^2 \rangle$ from the Monte Carlo simulations (white circle) for 20 ML $FePS_3$ as a function of temperature. b) Magnetic anisotropy as a function of thickness extracted from Monte Carlo simulation (red circles) and Bruno's model (gray diamonds). c) Experimental (upper) and calculated (lower) monolayer XA and XMLD spectra. d) Raman spectra of $FePS_3$ flakes on the ITO/Si substrate. P1 and P2 originated from the long-range magnetic order, according to the previous Raman paper. The peak marked with an asterisk is a signal from the ITO substrate.

We also noticed some X-ray-induced modifications in the XA spectra for thicknesses below 3 ML, which prevents the temperature-dependent analysis of X_M. In these cases, we may extract the magnetic anisotropy parameter K from Bruno's theory,[35] which links the anisotropy energy to $\frac{1}{4}\xi\hat{S}\cdot(\Delta L)$,[37] where for the present case the orbital moment anisotropy $\Delta L = (L_z - L_x)$ and spin moment $\hat{S}$ are obtained from the multiplet calculations by fitting the respective XA spectra at low temperature. Here, ξ is an atomic spin–orbit coupling constant, which has a value of 50 meV for Fe. Interestingly, we find that the K values obtained from Bruno model are similar with what we got from MC down to 4 ML (see the gray diamonds in Figure 3b). For the 3ML, we find only a small decrease of K in Bruno's model, 20.6 ± 0.3 meV/Fe, as compared to the large drop of K, 11 meV/Fe from the MC calculations. For the monolayer, Bruno model yields $K \approx 11.6 \pm 0.4$ meV with ΔL and $\hat{S}$ from the data shown in Figure 3c. We argue that this reduction in K in the lower thicknesses indicates an interface effect with the ITO, likely related with the electron transfer to the FePS$_3$.

The latter occurs due to a work function mismatch between the p-type semiconductor FePS$_3$[38] and the metallic ITO.[39] Including a charge transfer in our multiplet simulations is achieved by reducing the charge transfer energy Δ, the effective coupling potential V_{e_g}, V_{a1g}, and $V_{e_g^{\pi}}$ in H_{lmct} and ligand's crystal field H_L parameters (other parameters are kept the same as that of 20 ML). Such simulations indeed reproduce the changes in the XA spectra for the monolayer (Figure 3c) and further yield $\langle S_z \rangle = 1.29 \pm 0.01$ and $\langle L_z \rangle = 0.72 \pm 0.02$, matching the reduced X_M in the XMLD data. This reduction of the magnetic moments correlates well with the strongly reduced antiferromagnetic order peaks P$_1$ and P$_2$ in the Raman spectra of FePS$_3$ on the ITO substrate (Figure 3d). At the same time, these data show that care must be exercised when bringing 2D vdW materials in contact with a substrate. Similar effects are well known from other systems, such as supported molecules, e.g. ref. [40]. The present case demonstrates that the electron transfer effect is also relevant in 2D vdW materials on supports, but might have been overlooked thus far, because the commonly used experimental techniques lack the required sensitivity to such effects. In the present case, electron transfer from ITO to FePS$_3$ modifies the electronic and magnetic properties of the first few layers.

5. Spin–Orbit Entanglement

We note here that upon introducing spin–orbit coupling, the a$_{1g}$ and e$_g^{\pi}$ states are spin–orbit entangled (**Figure 4**b). Indeed, our multielectron calculations of FePS$_3$ reveal that the spin–orbit interaction leads to the spin–orbit entangled ground state of the $3d$ electronic system. In the multielectron calculations, we took a total Hamiltonian for the d^6 electrons of Fe^{2+} for the trigonal symmetry as detailed in the Supporting Information. We start the multielectron calculation from the cubic crystal electric field H_{CEF} with basis of $|L = 2, m_L\rangle$, because crystal electric field acts only on orbital moment. In our diagonalization of cubic H_{CEF}, we can start the calculation with the ground orbital triplet $^5T_{2g}$ state (i.e., $\tilde{L} = 1$ and $S = 2$) because the orbital moment of excited state E_g is zero and the energy splitting from T_{2g} to E_g is an order of eV. With the ground state $^5T_{2g}$, the simplified Hamiltonian can be described as $H = \lambda\tilde{L}\cdot S + \Delta_{trig}(\tilde{L}_z - \frac{2}{3})$, where λ is the spin–orbit coupling and Δ_{trig} is the trigonal distortion. Using the 15 basis functions of $(2\tilde{L}+1) \times (2S+1)$ in the $|\tilde{L}, S\rangle = |\tilde{L}=1\rangle_L \otimes |S=2\rangle_S$ basis, we calculate the ground state of FePS$_3$ by numerically diagonalizing the 15×15 matrix. By setting the $\lambda = 13$ meV and $\Delta_{trig} = -10$ meV from Quanty's best fit parameter value, multielectron calculation then produces a ground state of Fe^{2+} with the wave function of $|\Psi\rangle = \pm 0.8325|\mp1\rangle_L \otimes |\pm 2\rangle_S \mp 0.4712|0\rangle_L \otimes |\pm 1\rangle_S \pm 0.2914|\pm 1\rangle_L \otimes |0\rangle_S$, given in the $|L, S\rangle$ basis functions of $\tilde{L}=1$ and $S = 2$ for the six $3d$ electrons of Fe^{2+}. This ground state wave function cannot be factorized due to spin–orbit entanglement. Such complete mixing of all L–S basis functions is definitive evidence of spin-orbit entanglement for the ground state wave function. The entanglement would naturally couple the spin moment and the orbital moment, reinforcing the large magnetic anisotropy. We note that this wavefunction also has a large orbital moment of $\langle L_z \rangle = 0.6081$, which is close to the values from our multiplet calculations (see discussions further above) and consistent with
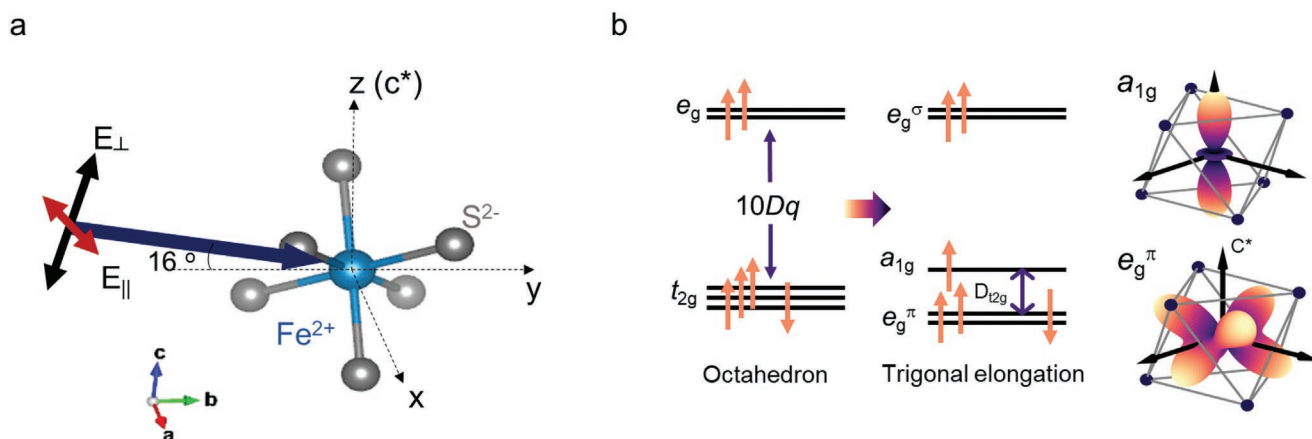

Figure 4. Geometry and electronic configuration considered in the multiplet calculations from Simulated XA spectra with different spin orientation. a) Schematic of the FeS$_6$ cluster and incident X-ray beam with linear polarization. The vectors of the incident X-ray beam and exchange field $\mathbf{H}_{ex}$ in the multiplet calculation are determined from this scheme. b) The high spin configuration under the crystal field (left). The e$_g^{\pi}$ and a$_{1g}$ orbitals are visualized (right).

the recent LDA+U calculations.[34] To confirm our conclusion about the spin–orbit entangled ground state, we analyzed the branching ratio of I_{L3}/I_{L2} of the experimental XA spectrum at 65 K. The quantity $I(L_{2,3})$ is the integrated intensity of the "white line" (colored area in Figure S8, Supporting Information) of the absorption spectrum in the Fe $L_{2,3}$ edge. Traditionally, the branching ratio of XAS data has been used as a strict test of spin–orbit entanglement.[41,42] As detailed in the Supporting Information, the branching ratio of our experimental data is 3.84, significantly higher than a case without entanglement, $I_{L3}/I_{L2} = 2$. We think this constitutes compelling evidence supporting the spin–orbit entanglement in FePS$_3$. Interestingly, the wavefunctions of the ground state have a distinct shape, as shown in Figure 4b, with e$_g^\pi$ having more prominent in-plane orbital moments.

At first glance, a spin–orbit entangled ground state in FePS$_3$ appears to be a surprising result, as the spin–orbit coupling is much weaker for $3d$ transition metal elements than systems based on Ir, Ru, and $4f$ elements. However, it is known that for certain conditions, even weak spin–orbit coupling can easily give rise to ground states with significant spin–orbit entanglement for several $3d$ transition metal elements. For instance, Co^{2+} ions are a case in point, as discussed in ref. [43]. Another example is an Ising metallic system Fe$_{1/4}$TaS$_2$.[17] This system also has a large magnetic anisotropy with unquenched orbital moments. The large magnetic anisotropy ≈ 14 meV/Fe originates from the same mechanism as FePS$_3$, combination of spin–orbit coupling and unquenched orbital moment ≈ 1 μ_B/Fe from trigonal distortion. Finally, additional optical data exhibit visible temperature-dependent spectral transfer in FePS$_3$ (see Figure S9, Supporting Information). A similar spectral transfer was recently considered evidence of a strong correlation in NiPS$_3$.[44] Thus, finding a spin–orbit entangled state in $3d$ transition metal compounds such as FePS$_3$ provides prominent new opportunities for investigating the potential effect of strong electron correlation on the final entangled ground state, most notably all on the 2D limit. It is entirely an open question how strong electron correlation impacts the spin–orbit entangled ground state of FePS$_3$, which will be the subject of future studies.

6. Conclusion

Our experiments demonstrate that orbital magnetism and spin–orbit entanglement play a key role in the enormous magnetic anisotropy and Ising-type magnetism of FePS$_3$. We obtain the sizeable magnetic anisotropy value of 22 meV/Fe from our analysis and demonstrate the existence of an unquenched orbital moment from multiplet calculations by fitting polarization- and temperature-dependent XA data. With the high-resolution XMLD mapping results, we can analyze the magnetic anisotropy's thickness dependence down to monolayer FePS$_3$. It is also crucial to note that the gigantic magnetic anisotropy is due to spin–orbit entanglement for Fe^{2+} under trigonal elongation: the Ising magnetism of FePS$_3$ is intrinsically a quantum phase with strong entanglement. Finally, we demonstrate an electron transfer effect at the interface between the ITO substrate and FePS$_3$. Being able to probe such effects is crucial for potential

applications of thin 2D vdW material layers. Therefore, we anticipate that our results will open the door to new investigations into quantum phases in 2D vdW magnets.

7. Experimental Section

Sample Preparation and Basic Characterization: FePS$_3$ single crystals were synthesized employing chemical vapor transport (CVT). The Fe, P, and S powders (99.99%, Alfa Aesar) were sealed into a quartz ampule. The sample was then placed in a horizontal two-zone furnace with temperatures of 750 °C (hot zone) and 730 °C (cold zone) and kept for 9 d. The magnetic susceptibility of bulk FePS$_3$ was measured using a commercial magnetometer (MPMS5, Quantum Design) (Figure S1, Supporting Information). The measurement was performed by field cooling with a 300 Oe magnetic field. Au markers were lithographically patterned on the ITO substrates and used to identify and locate selected FePS$_3$ flakes for correlating the same sample's XPEEM and AFM. FePS$_3$ flakes were mechanically exfoliated on an ITO (70 nm)/Si substrate, and AFM was used to determine the thickness of the exfoliated flakes. Exfoliation and AFM measurements were carried out in a glove box filled with Ar gas.

Before the main experiment of FePS$_3$, feasibility tests of XMLD-PEEM on different substrates was conducted. Since FePS$_3$ is insulating, eliminating the charging effect is crucial for obtaining the correct X-ray absorption coefficient. ITO and SiO$_2$ substrates were tried with a patterned gold window. In test experiments, the ITO substrate gave more stable images than the gold-patterned SiO$_2$ substrate.

Raman Measurement: Raman scattering measurements were carried out on the sample fabricated by the same method. An Ar-ion laser with a wavelength of 488 nm (2.54 eV) and a power of ≈ 50 μW was used. The substrate with the exfoliated samples was loaded into a He-flow optical cryostat (Oxford MicrostatHe2). The scattered light from the sample was dispersed using a Jobin-Yvon Horiba iHR550 spectrometer (2400 grooves mm^{-1}) and detected with a liquid nitrogen-cooled CCD.

X-ray Absorption and Magnetic Linear Dichroism Spectroscopy: The X-PEEM experiments were performed at the Surface/Interface Microscopy (SIM) beamline of the Swiss Light Source, Paul Scherrer Institute. Element-specific magnetic information at a spatial resolution of 50–100 nm was obtained by tuning the X-ray photon energy to the L_3 absorption edge of Fe. The experiment was performed from low to high temperatures to minimize X-ray-induced sample damage. ImageJ was used for image processing steps such as drift correction and normalization to extract the intensity from the region of interest and pixel-wise contrast calculations.

Recording sequences of XPEEM images at successive photon energies and as a function of polarization enables to acquire thickness- and polarization-dependent XA spectra to probe the anisotropic properties of the sample. The XA spectra were acquired by sequencing XA intensities from the XPEEM images at successive photon energies. A linear baseline correction was performed for each spectrum. Normalization was achieved by dividing each data point by the L_3 peak intensity. XPEEM elemental contrast maps were obtained by pixel-wise division of images recorded at the Fe L_3 peak ($h\nu = 708.5$ eV) and pre-edge energy ($h\nu = 704.2$ eV).

Magnetic contrast maps were obtained by pixel-wise evaluation of the normalized XMLD asymmetry $A = [I_\perp^{(C,B)} - I_\parallel^{(C,B)}]/[I_\perp^{(C,B)} + I_\parallel^{(C,B)}]$, where $I_\perp^{(C,B)}$ and $I_\parallel^{(C,B)}$ denote the ratio of the local absorption intensities at the respective photon energy for two different polarizations. The asymmetry is proportional to $\langle M_z^2 \rangle - \langle M_x^2 \rangle$, with $\langle M_{z,x}^2 \rangle$ being the expectation values of the squared order parameter with components perpendicular or parallel to the sample plane. Hence, a disordered state (static or dynamic) with $\langle M_{z,x}^2 \rangle = 0$ yields $A = 0$, while $A \neq 0$ indicates a common orientation of the atomic magnetic moments.

The magnetization- and polarization-dependent XA intensity can be described as $I(\mathbf{M,E}) = I_0 + c\ (\mathbf{E \cdot M})^2$, with I_0 ($h\nu$) being the isotropic,

photon energy $h\nu$ dependent XA, **E** being the polarization vector of linear polarized X-rays, **M** being the local order parameter, and $c = c(h\nu)$ being a photon energy-dependent parameter containing information about the microscopic magnetic properties of the sample.[45] The order parameter of FePS$_3$ is given by $\mathbf{M} = (\mathbf{M}\uparrow - \mathbf{M}\downarrow)/2$, where $\mathbf{M}\uparrow\downarrow$ corresponds to the total probed magnetization of the oppositely polarized Fe ion sublattices in the zig-zag chains. XPEEM images were taken with the X-ray polarization either parallel, $\mathbf{E}_\parallel = (E,0,0)$, or almost perpendicular to the sample plane, $\mathbf{E}_\perp = (0, E\cdot\sin\theta, E\cdot\cos\theta)$, and with $\theta = 16°$ being the angle of incidence of the X-rays (Figure 1b).

Simulation of XA Spectra: The quantum many-body program Quanty[46] was used to simulate XA spectra. The script language Quanty enables to calculate X-ray absorption spectra, defining operators in second quantization and calculating the eigenstates of Green's functions for these operators.[47] From calculating the eigenstates, the expectation value of ground state including $\langle L_{x,y,z}\rangle$ and $\langle S_{x,y}\rangle$ can be obtained. Quanty input files were generated by Crispy,[48] a graphical user interface core-level spectra simulation program. A ligand field multiplet model was used, considering the *pd*-hybridization of Fe *d*-orbitals and S *p*-orbitals in the FeS$_6$ cluster.[46] To reflect the trigonal elongation along the [111] direction of the FeS$_6$ cluster, D_{3d} Hamiltonian terms were added to the original Crispy input file. The calculated geometry, including the incident X-ray direction and E-field vector orientation, is shown in Figure 4a. The input parameters are free parameters, so their values were fitted to reproduce the experimental XA spectrum. The crystal field H_c and the *pd* hybridization terms, H_{lmct} and H_L, were adjusted to match the experimental XA spectra in the paramagnetic state at 300 K. The trigonal distortion parameter D_{t2g} is assigned to be -10 meV from the previous optical result.[49] An exchange field was applied parallel to the $c*$-axis direction to reproduce the magnetic state of FePS$_3$ below T_N. Other parameters were fixed to the parameters fitted at 300 K. This exchange field acts only on the spin moment and is defined as $H_{ex} = \sum_i J\langle S_i\rangle$.[50]

Increasing the exchange field H_{ex} along the *z*-direction induces an increase in $\langle S_z\rangle$ and $\langle L_z\rangle$ due to spin–orbit coupling. The increased *z*-component of the spin and orbital moments leads to boosted magnetic anisotropy (Figure S2a,b, Supporting Information). In addition, the normalized asymmetry X_M increases with a larger H_{ex} (Figure S2c, Supporting Information). The input parameters from the best fit are summarized in **Table 1**.

Monte Carlo Simulation: The magnetic properties were investigated through a Monte Carlo simulation. A classical 2D honeycomb lattice Heisenberg exchange model was used with strong local out-of-plane anisotropy based on the quantum spin Hamiltonian of refs. [30,51]. The Heisenberg exchange coupling includes up to the fourth nearest neighbor. Following ref. [51] only intralayer exchange interactions were considered: including an interlayer exchange interaction as in ref. [30] results in a minor change. Thus, the classical vdW material was modeled as a stack of noninteracting MLs, each described by

$$H = -\frac{1}{2}\sum_{ij} J_{ij}\hat{m}_i\cdot\hat{m}_j - K\sum_i (\hat{m}_{z,i})^2 \tag{4}$$

A Néel temperature of 125 K was obtained with the exchange parameters $J_1 = 14.6$, $J_2 = -0.4$, $J_3 = -9.6$, and $J_4 = -0.073$ meV and an out-of-plane anisotropy $K = 26.6$ meV. The corresponding ground-state exchange field is $H_{ex} \approx J_1 - 2J_2 - 3J_3 = 15$ meV. The ratios of these parameters were chosen equal to those of the quantum spin Hamiltonian found in ref. [30] ($J^{quantum}M^2 \sim J$), resulting in a classical moment magnitude estimate M compatible with that of Fe. For the study of the phase transition, a classical spin Hamiltonian is justified.

Table 1. Summary of parameters used for the Quanty simulation.

Hamiltonian	Parameters
Atomic terms H_d	$U_{dd} = 2.0$ eV
	$U_{pd} = 2.5$ eV
Crystal field H_c	$10Dq = 0.4$ eV
	$D_{t2g} = -0.01$ eV
Ligand–metal charge transfer H_{lmct}	$\Delta = 1.0$ eV
	$V_{a1g} = 2.3$ eV
	$V_{eg\pi} = 2.2$ eV
	$V_{eg\sigma} = 3.0$ eV
Ligand crystal field H_L	$10Dq^{lig} = 1.5$ eV
	$D_{t2g}^{lig} = -0.1$ eV

The Hamiltonian used in Quanty is $H_{tot} = H_d + H_c + H_{lmct} + H_L + H_{ex}$:
– Atomic terms H_d are for the Fe electrons' Coulomb interactions and spin–orbit coupling.
The on-site Coulomb repulsion in different *d*–*d* orbitals U_{dd}
Coulomb interaction between the 2*p*-core hole and 3*d*-electron U_{pd}
Slater integrals are reduced to 80% of the Hartree-Fock value with a spin–orbit coupling constant of $\xi = 0.05$ eV.
– Crystal electric field H_c reflects the splitting of Fe 3*d* orbitals by the crystal electric field (see Figure 4b).
Cubic crystal field $10\,Dq$ split Fe 3*d* orbitals into t$_{2g}$ and e$_g$ states.
D_{t2g} is a trigonal distortion parameter that splits the t$_{2g}$ orbitals into the e$_g^\pi$ and a$_{1g}$ states. D_{t2g} is defined as $E(e_g^\pi) - E(a_{1g})$. The negative D_{t2g} reflects the trigonal elongation, setting the doublet e$_g^\pi$ as a ground state.
By $10\,Dq$ and D_{t2g}, the energies of the Fe 3*d* orbitals are described as

$$E_{e_g^\sigma} = 0.6 \times 10Dq \tag{1}$$

$$E_{a1g} = -0.4 \times 10Dq - 2/3 \times D_{t2g} \tag{2}$$

$$E_{e_g^\pi} = -0.4 \times 10Dq + 2/3 \times D_{t2g} \tag{3}$$

– Ligand–metal charge transfer H_{lmct} is the Hamiltonian that considers the charge transfer effect from the S ligand to the Fe 3*d* metal.
Charge transfer energy Δ is the energy difference between d^6 and d^7L, where L denotes the S *p*-orbital hole states; $\Delta = E(d^7\underline{L}) - E(d^6)$.
The hopping between the S and Fe ions can be depicted as an effective potential coupling of two different orbitals. This effective potential coupling describes the Fe 3*d*-orbital energy states of D_{3d} symmetry, i.e., $V_{e_g^\pi}$, Va_{1g}, and $V_{e_g^\sigma}$.
– H_L is the sulfur ligand crystal electric field Hamiltonian.
Cubic crystal field parameter $10\,Dq^{lig}$ and trigonal distortion parameter D_{t2g}^{lig}

Conflict of Interest

The authors declare no conflict of interest.

Supporting Information

Supporting Information is available from the Wiley Online Library or from the author.

Data Availability Statement

The data that support the findings of this study are available from the corresponding author upon reasonable request.

[1] L. Onsager, *Phys. Rev.* **1944**, *65*, 117.

[2] J.-G. Park, *J. Phys. Condens. Matter* **2016**, *28*, 301001.

[3] K. S. Burch, D. Mandrus, J.-G. Park, *Nature* **2018**, *563*, 47.

[4] M. Gibertini, M. Koperski, A. F. Morpurgo, K. S. Novoselov, *Nat. Nanotechnol.* **2019**, *14*, 408.

[5] C. Gong, X. Zhang, *Science* **2019**, *363*, eaav4450.

[6] K. G. Wilson, *Rev. Mod. Phys.* **1983**, *55*, 583.

[7] J. U. Lee, S. Lee, J. H. Ryoo, S. Kang, T. Y. Kim, P. Kim, C. H. Park, J. G. Park, H. Cheong, *Nano Lett.* **2016**, *16*, 7433.

[8] C. Gong, L. Li, Z. Li, H. Ji, A. Stern, Y. Xia, T. Cao, W. Bao, C. Wang, Y. Wang, Z. Q. Qiu, R. J. Cava, S. G. Louie, J. Xia, X. Zhang, *Nature* **2017**, *546*, 265.

[9] B. Huang, G. Clark, E. Navarro-Moratalla, D. R. Klein, R. Cheng, K. L. Seyler, D. Zhong, E. Schmidgall, M. A. McGuire, D. H. Cobden, W. Yao, D. Xiao, P. Jarillo-Herrero, X. Xu, *Nature* **2017**, *546*, 270.

[10] A. R. Wildes, V. Simonet, E. Ressouche, G. J. McIntyre, M. Avdeev, E. Suard, S. A. J. Kimber, D. Lançon, G. Pepe, B. Moubaraki, T. J. Hicks, *Phys. Rev. B* **2015**, *92*, 224408.

[11] K. Kim, S. Y. Lim, J. U. Lee, S. Lee, T. Y. Kim, K. Park, G. S. Jeon, C. H. Park, J. G. Park, H. Cheong, *Nat. Commun.* **2019**, *10*, 345.

[12] A. Bedoya-Pinto, J.-R. Ji, A. K. Pandeya, P. Gargiani, M. Valvidares, P. Sessi, J. M. Taylor, F. Radu, K. Chang, S. S. P. Parkin, *Science* **2021**, *374*, 616.

[13] S. Y. Lim, K. Kim, S. Lee, J.-G. Park, H. Cheong, *Curr. Appl. Phys.* **2021**, *21*, 1.

[14] K. Kim, S. Y. Lim, J. Kim, J.-U. Lee, S. Lee, P. Kim, K. Park, S. Son, C.-H. Park, J.-G. Park, H. Cheong, *2D Mater.* **2019**, *6*, 041001.

[15] A. Wildes, H. M. Rønnow, B. Roessli, M. Harris, K. Godfrey, *Phys. Rev. B* **2006**, *74*, 094422.

[16] I. G. Rau, S. Baumann, S. Rusponi, F. Donati, S. Stepanow, L. Gragnaniello, J. Dreiser, C. Piamonteze, F. Nolting, S. Gangopadhyay, *Science* **2014**, *344*, 988.

[17] K.-T. Ko, K. Kim, S. B. Kim, H.-D. Kim, J.-Y. Kim, B. Min, J.-H. Park, F.-H. Chang, H.-J. Lin, A. Tanaka, *Phys. Rev. Lett.* **2011**, *107*, 247201.

[18] D. I. Khomskii, S. V. Streltsov, *Chem. Rev.* **2020**, *121*, 2992.

[19] B. Keimer, J. E. Moore, *Nat. Phys.* **2017**, *13*, 1045.

[20] J. Jensen, A. R. Mackintosh, *Rare Earth Magnetism*, Clarendon, Oxford, UK, **1991**.

[21] T. Jungwirth, X. Marti, P. Wadley, J. Wunderlich, *Nat. Nanotechnol.* **2016**, *11*, 231.

[22] V. Baltz, A. Manchon, M. Tsoi, T. Moriyama, T. Ono, Y. o. M. P. Tserkovnyak, *Rev. Mod. Phys.* **2018**, *90*, 015005.

[23] B. Huang, M. A. McGuire, A. F. May, D. Xiao, P. Jarillo-Herrero, X. Xu, *Nat. Mater.* **2020**, *19*, 1276.

[24] L. Thiel, Z. Wang, M. A. Tschudin, D. Rohner, I. Gutiérrez-Lezama, N. Ubrig, M. Gibertini, E. Giannini, A. F. Morpurgo, P. Maletinsky, *Science* **2019**, *364*, 973.

[25] H. Chu, C. J. Roh, J. O. Island, C. Li, S. Lee, J. Chen, J.-G. Park, A. F. Young, J. S. Lee, D. Hsieh, *Phys. Rev. Lett.* **2020**, *124*, 027601.

[26] F. Feringa, G. E. W. Bauer, B. J. van Wees, *Phys. Rev. B* **2022**, *105*, 214408.

[27] A. Farhan, P. Derlet, A. Kleibert, A. Balan, R. Chopdekar, M. Wyss, L. Anghinolfi, F. Nolting, L. J. Heyderman, *Nat. Phys.* **2013**, *9*, 375.

[28] A. F. Rodríguez, A. Kleibert, J. Bansmann, A. Voitkans, L. Heyderman, F. Nolting, *Phys. Rev. Lett.* **2010**, *104*, 127201.

[29] F. Nolting, A. Scholl, J. Stöhr, J. W. Seo, J. Fompeyrine, H. Siegwart, J.-P. Locquet, S. Anders, J. Lüning, E. Fullerton, *Nature* **2000**, *405*, 767.

[30] D. Lançon, H. C. Walker, E. Ressouche, B. Ouladdiaf, K. C. Rule, G. J. McIntyre, T. J. Hicks, H. M. Rønnow, A. R. Wildes, *Phys. Rev. B* **2016**, *94*, 214407.

[31] N. Chandrasekharan, S. Vasudevan, *Pramana* **1994**, *43*, 21.

[32] M. Nauman, D. H. Kiem, S. Lee, S. Son, J.-G. Park, W. Kang, M. J. Han, Y. J. Jo, *2D Mater.* **2021**, *8*, 035011.

[33] A. McCreary, J. R. Simpson, T. T. Mai, R. D. McMichael, J. E. Douglas, N. Butch, C. Dennis, R. V. Aguilar, A. R. H. Walker, *Phys. Rev. B* **2020**, *101*, 064416.

[34] T. Y. Kim, C.-H. Park, *Nano Lett.* **2021**, 10114.

[35] P. Bruno, *Phys. Rev. B* **1989**, *39*, 865.

[36] A. Kartsev, M. Augustin, R. F. L. Evans, K. S. Novoselov, E. J. G. Santos, *NPJ Comput. Mater.* **2020**, *6*, 150.

[37] G. van der Laan, *J. Phys.: Condens. Matter* **1998**, *10*, 3239.

[38] A. Aruchamy, H. Berger, F. Levy, *J. Solid State Chem.* **1988**, *72*, 316.

[39] Y. Park, V. Choong, Y. Gao, B. R. Hsieh, C. W. Tang, *Appl. Phys. Lett.* **1996**, *68*, 2699.

[40] C. Wäckerlin, K. Tarafder, D. Siewert, J. Girovsky, T. Hählen, C. Iacovita, A. Kleibert, F. Nolting, T. A. Jung, P. M. Oppeneer, *Chem. Sci.* **2012**, *3*, 3154.

[41] D.-Y. Cho, J. Park, J. Yu, J.-G. Park, *J. Phys. Condens. Matter* **2012**, *24*, 055503.

[42] J. P. Clancy, N. Chen, C. Y. Kim, W. F. Chen, K. W. Plumb, B. C. Jeon, T. W. Noh, Y.-J. Kim, *Phys. Rev. B* **2012**, *86*, 195131.

[43] A. Abragam, B. Bleaney, *Electron Paramagnetic Resonance of Transition Ions*, Oxford University Press, Oxford, UK **1970**.

[44] S. Y. Kim, T. Y. Kim, L. J. Sandilands, S. Sinn, M.-C. Lee, J. Son, S. Lee, K.-Y. Choi, W. Kim, B.-G. Park, J.-G. Park, H. Cheong, *Phys. Rev. Lett.* **2018**, *120*, 136402.

[45] A. Scholl, J. Stöhr, J. Lüning, J. W. Seo, J. Fompeyrine, H. Siegwart, J.-P. Locquet, F. Nolting, S. Anders, E. Fullerton, *Science* **2000**, *287*, 1014.

[46] M. W. Haverkort, M. Zwierzycki, O. K. Andersen, *Phys. Rev. B* **2012**, *85*, 165113.

[47] F. M. de Groot, H. Elnaggar, F. Frati, R.-P. Wang, M. U. Delgado-Jaime, M. van Veenendaal, J. Fernandez-Rodriguez, M. W. Haverkort, R. J. Green, G. van der Laan, *J. Electron Spectrosc. Relat. Phenom.* **2021**, *249*, 147061.

[48] M. Retegan, Crispy: v0.7.3, **2019**, https://doi.org/10.5281/zenodo.1008184.

[49] P. Joy, S. Vasudevan, *Phys. Rev. B* **1992**, *46*, 5134.

[50] M. W. Haverkort, S. I. Csiszar, Z. Hu, S. Altieri, A. Tanaka, H. H. Hsieh, H. J. Lin, C. T. Chen, T. Hibma, L. H. Tjeng, *Phys. Rev. B* **2004**, *69*, 020408.

[51] A. R. Wildes, K. C. Rule, R. I. Bewley, M. Enderle, T. J. Hicks, *J. Phys. Condens. Matter* **2012**, *24*, 416004.